$\mathcal{H}_\infty$ and μ-Synthesis for Nanosatellites Rendezvous and Docking

Camille Pirat, Finn Ankersen, *Member, IEEE*, Roger Walker, and Volker Gass

***Abstract*— In this brief, the nanosatellite rendezvous and docking problem is tackled. It was never attempted for small spacecraft, as critical technologies, such as six-degree-of-freedom (DoF) micropropulsion systems, have only recently become available due to advances in MEMS. The typical level of noise in nanosatellites' sensors and actuators combined with the dynamics uncertainties, low actuation capabilities, and reliability requirements makes the use of robust control appropriate. The system is described by a linearized rotation/translation, six DoFs, and coupled dynamics, including fuel sloshing. An $\mathcal{H}_\infty$ controller is first designed, in which robust stability and performance are assessed using structured singular values. The controller robustness is then improved using μ-synthesis. Nonlinear Monte Carlo simulations for both controllers, including realistic sensors and actuators models, are provided allowing a thorough assessment of the complete guidance, navigation and control (GNC). The sought GNC schemes are shown to be robust to the modeled uncertainties and to satisfy the docking requirements.**

***Index Terms*— Cubesats, docking, $\mathcal{H}_\infty$, μ-analysis, μ-synthesis, rendezvous, robust control, satellites.**

I. Introduction

ROBUSTNESS in space has always been of significant concern in the design of space systems, whether for the conception of telecommunication hardware, scientific payload, or navigation and control algorithms. This is especially true for rendezvous and docking (RVD) missions, for which a failure could have catastrophic consequences. RVD is a procedure during which a satellite, called the chaser, is being maneuvered toward and attached to another satellite, the target, by a succession of open-loop and closed-loop maneuvers. The docking of two satellites requires a high control accuracy and has always been challenging. For European Space Agency (ESA) own Automated Transfer Vehicle (ATV), a lateral accuracy better than 10 cm was required with a relative angular alignment better than 5° [1].

In 1999, a new class of satellites were created, called CubeSats. These nanosatellites weigh between 1 and 20 kg and satisfy a specific form factor called a unit, a $10 \times 10 \times 10$-cm cube. With the growing amount of available CubeSat technologies, RVD can finally be envisaged for these types of nanosatellites but was yet never attempted. For CubeSats, the required relative position and attitude accuracy to dock are estimated to be 1 cm and 2° [2].

Today, only a few spacecraft have performed RVD, and three of them are of paramount importance and represent the state of the art: the Russian Soyuz and Progress, and the European ATV. The first two vehicles are based on nonlinear control and pulsed linearization [3], whereas ATV is based on a six-degree-of-freedom (DoF) linear coupled dynamics and is using an $\mathcal{H}_\infty$ controller and pulse width modulation (PWM)-operated thrusters for the actuation [4].

Earlier in the development of the ATV, several control algorithms were investigated, among which are linear quadratic Gaussian (LQG) control, Pole Placement, $\mathcal{H}_\infty$, and μ-synthesis [5]. These all suggested promising performances, although the robust controllers were more efficient at dealing with the flexible solar arrays. $\mathcal{H}_\infty$, linear quadratic regulator (LQR), and proportional-integral-derivative controller have also been traded off for a docking experiment taking place within the International Space Station (ISS) using the MIT SPHERES [6]. More optimal solutions have been sought using linear quadratic tracking and state-dependent Riccati equation control algorithms, although the coupling between the rotations and translations has not been explicitly considered [7]. Model predictive control schemes have also been investigated for docking with a fixed [8] or a rotating [9] target.

The level of CubeSat-specific challenges, such as sensor and actuators' noise, low actuation capability, and dynamics uncertainties, combined with the required level of reliability, naturally leads to the use of robust control schemes, such as $\mathcal{H}_\infty$ or μ-synthesis. Furthermore, robust control had a successful on-orbit application in the frame of the ATV program, upon which this brief is built and extends the results.

The issue of uncertainties in the feedback system can be addressed using $\mathcal{H}_\infty$ control. It has been applied to a variety of subjects among which is the control of space systems with flexible appendages, such as for large space structures [10] or for satellites with large solar arrays or antennas [11]. Robustness can be efficiently assessed using structured singular values (SSVs) and has recently been proven to be more efficient than Monte Carlo at detecting destabilizing combinations of parameters [12]. As a way to further improve robustness, μ-synthesis can be used. This control method has been investigated for the position and attitude control of the ATV [5] and was shown to be more robust than $\mathcal{H}_\infty$.

Although RVD and robust control are well-understood problems for large spacecraft, a clear gap exists with CubeSats and nanosatellites. A first step has been taken in [6] in the frame of the SPHERES experiment. However, the dynamics

Manuscript received November 2, 2018; accepted December 25, 2018. Date of publication February 5, 2019; date of current version April 13, 2020. Manuscript received in final form January 10, 2019. This work was supported by the European Space Agency Networking/Partnering Initiative (NPI) Program under Contract 4000112462/14/NL/GLC. Recommended by Associate Editor M. Ariola. *(Corresponding author: Camille Pirat.)*

C. Pirat and V. Gass are with the Swiss Space Center, Swiss Federal Institute of Technology in Lausanne, 1015 Lausanne, Switzerland (e-mail: camille.pirat@epfl.ch; volker.gass@epfl.ch).

F. Ankersen and R. Walker are with the European Space Research and Technology Centre, European Space Agency, 2201AZ Noordwijk, The Netherlands (e-mail: finn.ankersen@esa.int; roger.walker@esa.int).

Color versions of one or more of the figures in this article are available online at http://ieeexplore.ieee.org.

Digital Object Identifier 10.1109/TCST.2019.2892923

1063-6536 © 2019 IEEE. Translations and content mining are permitted for academic research only. Personal use is also permitted, but republication/redistribution requires IEEE permission. See https://www.ieee.org/publications/rights/index.html for more information.

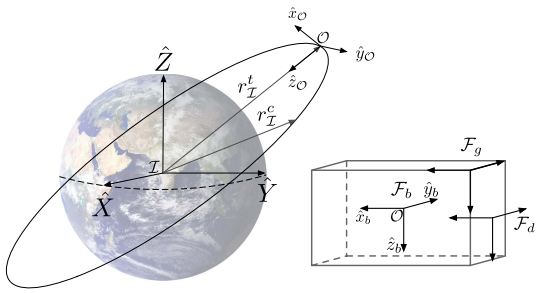

Fig. 1. Reference frames.

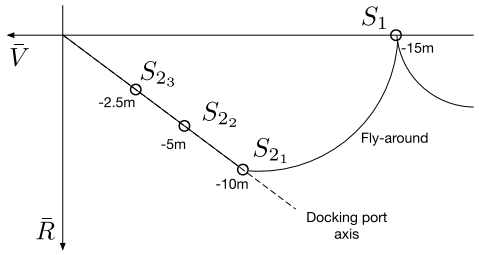

Fig. 2. RVD scenario.

and level of external perturbations are distinctly different than for an actual space mission, as this experiment took place within the controlled environment of the ISS. This brief then aims at providing a more comprehensive answer to this control problem. The most advanced research has been performed in the frame of the ATV in [4] in which a comprehensive robust control solution based on $\mathcal{H}_\infty$ and μ-analysis was proposed. This will be used as a starting point to design the controllers.

II. Problem Formulation

Five different reference frames are needed to define the problem properly. They are shown in Fig. 1. The Earth-centered inertial frame, $\mathcal{F}_\mathcal{I}$, is centered on the Earth and has the X-axis toward the vernal equinox and uses the J2000 definition [13]. The Z-axis points toward the North pole, and $\hat{Y}$ completes the direct triad. $\boldsymbol{r}^t_\mathcal{I}$ and $\boldsymbol{r}^c_\mathcal{I}$ are the target and chaser satellites' inertial position.

The local-vertical/local-horizontal frame, $\mathcal{F}_\mathcal{O}$, is centered on the satellite centre of mass (CoM): $\hat{z}_\mathcal{O} = -(\boldsymbol{r}/r,)$ where $\boldsymbol{r}$ is the satellite position in $\mathcal{F}_\mathcal{I}$ and is referred to as $\bar{R}$. $\hat{y}_\mathcal{O} = -(\boldsymbol{r} \times \boldsymbol{v})/(|\boldsymbol{r} \times \boldsymbol{v}|,)$ where $\boldsymbol{v}$ is the satellite velocity in $\mathcal{F}_\mathcal{I}$ and is called $\bar{H}$. Finally, $\hat{x}_\mathcal{O}$ completes the direct frame and is referred to as $\bar{V}$.

The remaining frames are: the geometrical frame, $\mathcal{F}_g$, the body frame, $\mathcal{F}_b$, which has its origin on the satellite CoM, and the docking frame, $\mathcal{F}_d$. Note that for these frames, the subscripts c or t can be added to differentiate the chaser's frames from the target's frames.

A typical RVD scenario is provided in Fig. 2. The objective is to control the relative position and orientations between the two satellites' docking ports. The port-to-port (P2P) control will start at point S_{2_1}, at 10-m range, once the chaser is already aligned with the target port. How to bring the chaser satellite to this point for specific CubeSat applications has been discussed

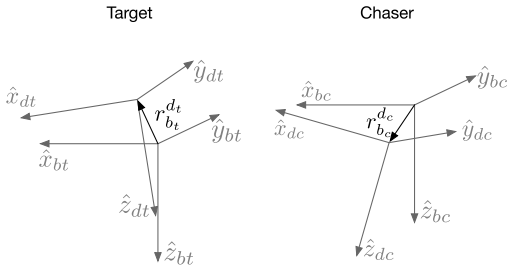

Fig. 3. Body frame $\mathcal{F}_b$ and docking port frame $\mathcal{F}_d$ for the target and chaser satellites.

in [14]. The guidance from S_{2_1} to S_{2_2}, S_{2_2} to S_{2_3}, and finally to docking is a forced straight line motions at a speed of 1 cm/s.

A. Relative Attitude

The dynamics used in this brief are an improved version than the one proposed in [4] and can be found in [15]. It is briefly recalled here. Fig. 3 shows the docking port frames in their respective satellites. $\boldsymbol{r}^{d_t}_{b_t}$ is the position of the target docking port expressed in the target body frame $\mathcal{F}_{b_t}$ and $\boldsymbol{r}^{d_t}_{d_t} = A_{d_t b_t}\, \boldsymbol{r}^{d_t}_{b_t}$, where $A_{d_t b_t}$ is a direction cosine matrix mapping $\mathcal{F}_{b_t}$ to $\mathcal{F}_{d_t}$. The attitude dynamics expressed in an arbitrary frame $\mathcal{F}_d$ is

$$\dot{\boldsymbol{\omega}}^{do}_d = I_d^{-1}\left[\boldsymbol{T}_d - \left(\boldsymbol{\omega}^{do}_d + A_{do}\, \boldsymbol{\omega}^{oI}_o\right) \times \left(I_d\left(\boldsymbol{\omega}^{do}_d + A_{do}\, \boldsymbol{\omega}^{oI}_o\right)\right)\right] \tag{1}$$

with $A_{do} = A_{db}A_{bo}$, $\boldsymbol{T}_d$ is the torque control input, $\boldsymbol{\omega}^{do}_d$ is the docking port rotation rate with respect to $\mathcal{F}_\mathcal{O}$, and $\boldsymbol{\omega}^{oI}_o$ is the rotation rate of $\mathcal{F}_\mathcal{O}$ with respect to $\mathcal{F}_\mathcal{I}$, expressed in $\mathcal{F}_\mathcal{O}$: $\boldsymbol{\omega}^{oI}_o = [0\ -\omega_o\ 0]^{\mathrm{T}}$, with ω_o the orbital mean motion. I_d is the satellite inertia in $\mathcal{F}_d$ and is obtained from the known inertia in the body frame I_b

$$I_d = A_{db}\left(I_b + m\left[\left\|\boldsymbol{r}^d_b\right\|^2 I_3 - \boldsymbol{r}^d_b \boldsymbol{r}^{d^{\mathrm{T}}}_b\right]\right)A^{\mathrm{T}}_{db}. \tag{2}$$

The relative rotation rate between the chaser and target docking ports is then expressed in the chaser docking frame $\mathcal{F}_{d_c}$

$$\boldsymbol{\omega}^{d_c d_t}_{d_c} = \boldsymbol{\omega}^{d_c o}_{d_c} - A_{d_c d_t}\boldsymbol{\omega}^{d_t o}_{d_t} \tag{3}$$

with $\boldsymbol{\omega}^{d_c o}_{d_c}$ and $\boldsymbol{\omega}^{d_t o}_{d_t}$ dynamics given by (1). Differentiating (3) leads to the relative attitude dynamics equation

$$\dot{\boldsymbol{\omega}}^{d_c d_t}_{d_c} = \dot{\boldsymbol{\omega}}^{d_c o}_{d_c} - A_{d_c d_t}\dot{\boldsymbol{\omega}}^{d_t o}_{d_t} + \boldsymbol{\omega}^{d_c d_t}_{d_c} \times \left(A_{d_c d_t}\boldsymbol{\omega}^{d_t o}_{d_t}\right) \tag{4}$$

which contains the torques' input from the target and the chaser. The attitude angles $\boldsymbol{\alpha}^{d_c d_t} = [\alpha^{d_c d_t},\ \beta^{d_c d_t},\ \gamma^{d_c d_t}]^{\mathrm{T}}$ are represented using the 1-2-3 Euler sequence.

B. Relative Position

Fig. 4 shows the relative position between the chaser and target CoMs $\boldsymbol{s}^{ct}_I$, and the P2P position $\boldsymbol{s}^{d_c d_t}_I$. The P2P position can be expressed in $\mathcal{F}_{d_t}$ as

$$\boldsymbol{s}^{d_c d_t}_{d_t} = A_{d_t o}A_{oI}\boldsymbol{s}^{ct}_I + A_{d_t d_c}A_{d_c b_c}\boldsymbol{r}^{d_c}_{b_c} - A_{d_t b_t}\boldsymbol{r}^{d_t}_{b_t} \tag{5}$$

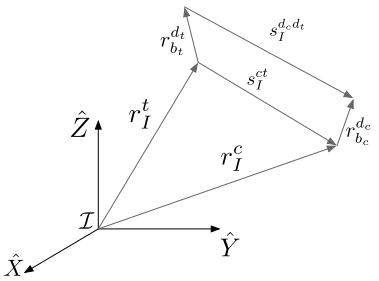

Fig. 4. Chaser and target relative position in $\mathcal{F}_\mathcal{I}$, and P2P relative position.

which can be differentiated two times to get the dynamics and the chaser translation control input $\boldsymbol{F}_{d_c}$. The state space has the following state vector:

$$\boldsymbol{x} = \left[\boldsymbol{\alpha}^{d_c d_t},\ \boldsymbol{\omega}_{d_c}^{d_c d_t},\ \boldsymbol{s}_{d_t}^{d_c d_t}, \dot{\boldsymbol{s}}_{d_t}^{d_c d_t}\right]^{\mathrm{T}} \tag{6}$$

where $\boldsymbol{\alpha}^{d_c d_t}$ and $\boldsymbol{\omega}_{d_c}^{d_c d_t}$ are the P2P relative Euler angles and rotation rates. The control input

$$\boldsymbol{u} = [\boldsymbol{T}_{d_c},\ \boldsymbol{F}_{d_c}]^{\mathrm{T}} \tag{7}$$

contains the chaser torques and force inputs expressed in the docking port frame. The units for the state vector are: rad, rad/s, m, and m/s. For the control input, units are Nm and N. The dynamics is linearized around $\boldsymbol{x} = \boldsymbol{0}$ and $\boldsymbol{u} = \boldsymbol{0}$, which is an equilibrium point if and only if $\mathcal{F}_{d_t} = \mathcal{F}_{b_t} = \mathcal{F}_\mathcal{O}$. The state-space A and B matrices have the following shape (if not specified otherwise, all matrix elements have dimension 3×3):

$$A = \begin{bmatrix} 0 & A_{12} & 0 & 0 \\ A_{21} & A_{22} & 0 & 0 \\ 0 & 0 & 0 & I_3 \\ A_{41} & A_{42} & A_{43} & A_{44} \end{bmatrix}, \quad B = \begin{bmatrix} 0 & 0 \\ B_{21} & 0 \\ 0 & 0 \\ B_{41} & B_{42} \end{bmatrix} \tag{8}$$

and are detailed in [15]. Finally, $C = I_{12}$ and $D = 0$.

The target attitude dynamics uses the full body dynamics as opposed to the one used for the ATV, where the ISS motion was represented by a harmonic oscillator [4]. Also, the controllability matrix $\mathcal{C} = [B\ AB\ A^2B\ \ldots\ A^{n-1}B]$, using the dynamics proposed in [4], is rank deficient, whereas it has full rank using the dynamics described earlier. This difference comes from the coupling between the target attitude and chaser position, which is here directly accounted for in the A and B matrices.

C. Sloshing

The sloshing dynamics is approximated by a spring-mass and damper model [4]. The liquid mass m_l is divided into a sloshing part, m_1, and a solid part, m_0, which does not contribute to the sloshing effect. As, to the best of our knowledge, no studies focused on sloshing for CubeSats propulsion systems, the ATV values will be used and correspond to a spherical tank with conical baffle. The transfer function relating an external force F_1 acting on the satellite and, F_s, the sloshing perturbation, is

$$\frac{F_s}{F_1} = \frac{c_s s + k_s}{s^2 + \frac{c_s}{m_1} s + \frac{k_s}{m_1}}. \tag{9}$$

TABLE I
P2P DYNAMICS' POLES, DAMPING ξ, AND NATURAL FREQUENCY ω

Poles	ξ	ω (rad/s)
$1.00 \cdot 10^{-19} \pm 7.08 \cdot 10^{-12} i$	$-1.42 \cdot 10^{-08}$	$7.08 \cdot 10^{-12}$
$-3.16 \cdot 10^{-20} \pm 4.27 \cdot 10^{-05} i$	$7.39 \cdot 10^{-16}$	$4.27 \cdot 10^{-05}$
$\pm 5.74 \cdot 10^{-04} \pm 1.26 \cdot 10^{-04} i$	$\mp 9.77 \cdot 10^{-01}$	$5.88 \cdot 10^{-04}$
$6.78 \cdot 10^{-20} \pm 1.08 \cdot 10^{-03} i$	$-6.26 \cdot 10^{-17}$	$1.08 \cdot 10^{-03}$
$-5.42 \cdot 10^{-20} \pm 1.08 \cdot 10^{-03} i$	$5.01 \cdot 10^{-17}$	$1.08 \cdot 10^{-03}$
$-1.36 \cdot 10^{-02} \pm 3.75 \cdot 10^{-05} i$	1.00	$1.36 \cdot 10^{-02}$
$-1.36 \cdot 10^{-02}$	1.00	$1.36 \cdot 10^{-02}$
$-7.99 \cdot 10^{-01} \pm 2.20 \cdot 10^{-03} i$	1.00	$7.99 \cdot 10^{-01}$
$-7.99 \cdot 10^{-01}$	1.00	$7.99 \cdot 10^{-01}$

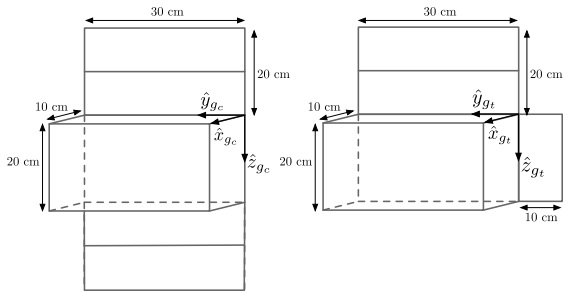

Fig. 5. Chaser (left) and target satellites. Their respective body frames are located at their center and aligned with $\mathcal{F}_{g_c}$ and $\mathcal{F}_{g_t}$.

In [4], the values for a half-full tank are $c_s \in [0.16;\ 0.5]$ s^{-1} and the natural frequency range is [0.01; 0.04] Hz.

The environmental perturbations are not directly accounted for in the dynamics, as they are attitude and position dependent. These are composed of the residual atmospheric drag, gravity gradient, and residual magnetic dipole [13]. Simulations show that the norms of the torques' and forces' perturbations are on average 1 μNm and 10 μN. They will be specifically included in the μ-analysis and Monte Carlo simulations. The poles of the plant are provided in Table I. The zeros are: -1.12, -1.35, $-1.31 \cdot 10^{-2} \pm 2.63 \cdot 10^{-5} i$, and $-1.12 \pm 1.44 \cdot 10^{-3} i$.

D. CubeSats Configuration

The two CubeSats are shown in Fig. 5 and satisfy the 6U CubeSats form factor. Both are equipped with deployable solar arrays. No information about their natural frequency content is available, but it is assumed to be high enough to be safely neglected. The target does not carry any fuel and weighs 11 kg. The chaser has a dry mass of 10 kg and carries 2 kg of propellant. To maximize the sloshing perturbations, a tank filling ratio of 1/2 is selected. It is believed that using the ATV values for the sloshing will lead to conservative results. The chaser's fuel is liquid butane, and the natural frequency of this system due to the tank size is expected to be higher than the ATVs. Both satellites are equipped with reaction wheels delivering 2 mNm around each axis with an output error of 10%. The chaser is further equipped with a cold gas propulsion system delivering 4 mN of thrust in each direction and has an output error of 10%. A related torque error is also

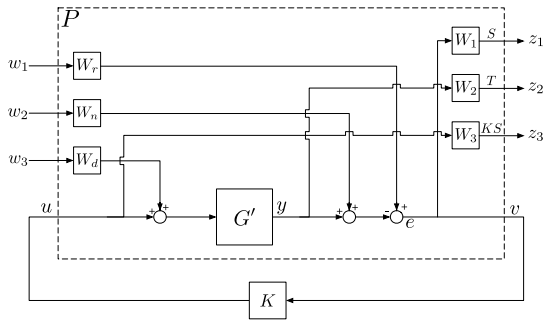

Fig. 6. S, T, and KS mixed sensitivity.

present (due to misalignment, timing error, and CoM uncertainties) amounting 5% of the thrust. To increase the coupling between rotations and translations, the ports are positioned so that their axes do not run through the satellites' CoMs. These positions in $\mathcal{F}_{b_t}$ and $\mathcal{F}_{b_c}$ are $\boldsymbol{r}_{b_t}^{d_t} = [-0.1\ 0.1\ 0.1]^{\mathrm{T}}$ m and $\boldsymbol{r}_{b_c}^{d_c} = [0.1\ 0.1\ 0.1]^{\mathrm{T}}$ m, respectively. Their orientations are such that $A_{d_c b_c} = A_{d_t b_t} = I_3$. Although these positions are out of the CubeSats, they represent a worst case and will increase coupling effects.

III. $\mathcal{H}_\infty$ Design

A relative accuracy of 1 cm and 2° (3σ) is required at docking. To have margins on the requirements, the lateral relative position control accuracy shall be better than 5 mm (3σ), and the relative attitude angles better than 1° (3σ). During translations, the relative position control shall be smaller than 5% of the range (3σ), and the relative attitude angles smaller than 2° (3σ). These requirements will be used for the definitions of the frequency-dependent weights during the synthesis of the $\mathcal{H}_\infty$ controller.

The mixed-sensitivity approach is used to solve the $\mathcal{H}_\infty$ problem, and the output sensitivity (S), complementary sensitivity (T), as well as the gain times sensitivity (KS) will be shaped [16]. The problem is shown in Fig. 6. G is transformed into an augmented plant P with three exogenous inputs $w_{1,\ldots,3}$ (reference signal, sensor noise, and input disturbances) and three exogenous outputs $z_{1,\ldots,3}$ (control error e, plant output y, and control signal u). The plant G is given by the state-space matrices (8). The D matrix is zero and

$$C = \begin{bmatrix} I_3 & 0 & 0 & 0 \\ 0 & 0 & I_3 & 0 \end{bmatrix} \tag{10}$$

meaning that only the relative position and attitude angles are available for feedback. This dynamic is then combined with the sloshing model to form the plant G. Note that if $C = I_{12}$ would have been selected instead, i.e., with the full state available for feedback, the output loop gain L would be rank deficient.

As, within the $\mathcal{H}_\infty$ framework, normalized signals are used, the plant G needs to be properly scaled. The input and output scaling matrices, U and Y, are such that

$$G' = Y^{-1} G U, \quad K_1 = U K Y^{-1} \tag{11}$$

where K_1 is the unscaled controller used for implementation and G' is the scaled plant. The U scale can be defined merely based on the available torques and forces. To avoid actuators' saturation, the values of 1 mNm and 1 mN are selected. The relative attitude angles should always remain constant and equal to zero; the attitude output is thus not scaled. The kinetic energy in the system is equal to the work of the actuation force: $(1/2)mv^2 = Fx$. While docking, the speed is 1 cm/s. Assuming that all the fuel has been depleted and that a 1-mN force is used, the actuation force, most important contribution, takes place at a distance $x = 0.5$ m. The input and output scaling matrices are thus

$$U = \begin{bmatrix} 10^{-3} I_3 & 0 \\ 0 & 10^{-3} I_3 \end{bmatrix}, \quad Y = \begin{bmatrix} I_3 & 0 \\ 0 & 0.5\ I_3 \end{bmatrix}. \tag{12}$$

A. Weights' Definition

W_r represent the frequency content of the reference signal and is selected as $W_r = I_6$. The state is estimated using a vision-based navigation (VBN) [15]. The navigation filter output is assumed to be a white noise with a 1° error for the relative attitude and 1% error for the relative position

$$W_n = \begin{bmatrix} \frac{180}{\pi} I_3 & 0 \\ 0 & 10^{-2} I_3 \end{bmatrix}. \tag{13}$$

Note that W_n attitude component is not unit-less, as the corresponding plant output is not scaled. As for the LQG, the $\mathcal{H}_\infty$ structure contains a separate estimator-like term, and the position and attitude could be directly filtered within the $\mathcal{H}_\infty$. This was not possible to do here, as the VBN measurement equations are varying with the range. The extended Kalman filter used for the VBN should, however, not impact the $\mathcal{H}_\infty$ phase margin (PM) and gain margin (GM), as, when combined to an LQR, the resulting LQG margins are preserved. This gives confidence that the VBN will not impact the $\mathcal{H}_\infty$ robustness. Finally, according to Section II-D, the actuators' uncertainties can be represented as

$$W_d = \left[\begin{array}{ccc|ccc} 0.1 & 0 & 0 & 0 & 0.05 & 0.05 \\ 0 & 0.1 & 0 & 0.05 & 0 & 0.05 \\ 0 & 0 & 0.1 & 0.05 & 0.05 & 0 \\ \hline 0 & 0 & 0 & 0.1 & 0 & 0 \\ 0 & 0 & 0 & 0 & 0.1 & 0 \\ 0 & 0 & 0 & 0 & 0 & 0.1 \end{array}\right]. \tag{14}$$

The top-right matrix block represents the thruster-related torques' errors. These three weighting matrices were kept simple so as to lower the controller order.

The required performances of the controller are defined using the weights $W_{1,\ldots,3}$. The performance weight W_1 is selected as a diagonal matrix, in which elements are the first-order transfer functions

$$W_{1_{i,i}}(s) = \frac{\frac{1}{M_1} s + \omega_1}{s + \omega_1 A_1}, \quad i = 1, \ldots, 6. \tag{15}$$

The mapping between the performance weight W_1 and the requirements is achieved by tuning M_1, A_1, and ω_1. Looking

only at the first exogenous input and output and as $W_r = I_6$: $z_1 = W_1 S w_1$. The steady-state error ($s = 0$) is thus defined as

$$W_{1_{i,i}}(s=0) = \frac{1}{A_1} = \frac{r_{\max}}{e_{\max}}. \tag{16}$$

As for this mission, a 5% error is required, $A_1 = 0.05$. At high frequencies, M_1 is bounding the sensitivity function from above. An overshoot smaller than 50% is required. Using the maximum peak criteria [16], this leads to $M_S = 2.5$. To have margins, a nominal overshoot of ∼30% is selected, which leads to $M_1 = 2$. Finally, ω can be approximated by $\omega \approx 4/t_s$, where t_s is the settling time [4]. The translation time from 2.5-m range to docking takes 225 s. A 100-s settling time is required. However, an 80-s time was selected to have margins with respect to the performance requirement. This leads to $\omega_1 = 0.1$ rad/s, which is below 0.25 rad/s of the sloshing modes and well above the dynamics' bandwidth (∼0.001 rad/s).

W_2 has the same diagonal structure than W_1

$$W_{2_{i,i}}(s) = \frac{s + \omega_2 A_2}{\frac{1}{M_2}s + \omega_2}, \quad i = 1, \ldots, 6. \tag{17}$$

To leave sufficient freedom to the $\mathcal{H}_\infty$ solver, $\omega_2 = 20\omega_1$ is selected. The weight should roll off to −20 dB to avoid noise amplification leading to $M_2 = 10$. At low frequency, $A_2 = 0.05$ which means that $\|T\|_\infty \leq 26$ dB. Theoretically, T should also be bounded by 6 dB, as S is. However, it was realized that giving the solver more freedom allowed achieving higher margins. Last, the input control weight is

$$W_{3_{i,i}}(s) = \frac{\frac{1}{M_3}s + \omega_3}{s + \omega_3 A_3}, \quad i = 1, \ldots, 6. \tag{18}$$

To not penalize the control input at low frequencies, $A_3 = 10^3$. The crossover frequency is selected as $\omega_3 = \omega_2$. Above this value, the weights roll off to −40 dB, $M_3 = 10^{-2}$, limiting high-frequency disturbances at the plant input.

Solving the suboptimal $\mathcal{H}_\infty$ problem, using the MATLAB Robust Control Toolbox [17], leads to $\gamma = 1.02$ with a 36-order controller. Simulations show that this controller does not meet the accuracy requirements. The reason is that $W_r = I_6$, meaning that changes at any frequency may happen, including infinitely fast changing reference signals. The controller was thus synthesized such that the maximum control output would be delivered for a step reference signal. To meet the performance requirements, the input scale U (12) is increased to give the controller more authority. This may lead to actuator saturation. However, the reference signal does not have high-frequency content, which limits possible saturation. W_r is also replaced by a transfer function similar to (15), and thus, it penalizes high-frequency contents in the reference. This increases the PM and GM considerably. The new input scale is: $U = \text{diag}[2{\cdot}10^{-3} I_3,\ 3{\cdot}10^{-2} I_3]$. All the other weights are identical to the first case where $W_r = I_6$. W_r parameters are: $M_r = 10^3$, $A_r = 0.8$, and $\omega_r = \omega_{2\&3}$ rad/s. This crossover frequency was selected such that W_r does not penalize signals before W_2 and W_3 do.

These new scaling matrices and weights lead to $\gamma = 0.77$, with GM = $[-4.6, 6.5]$ dB, PM = ±30.4°, and $\omega_c = 0.20$ rad/s at the input, and GM = $[-11.4, 13.7]$ dB, PM = ±46.7°, and $\omega_c = 0.13$ rad/s at the output. However, as W_r is now a 6×6 nontrivial diagonal matrix, the controller order grew from 36 to 42. The scaled plant and controller singular values are shown in Fig. 7(a). Here, KSWr > 0 dB and, thus, may lead to noise amplification at the plant input. However, when unscaling the plant, as shown in Fig. 7(b), KSWr < 0 dB, which guarantees no noise amplification. This controller shows good performances and meets the docking requirements. Note that increasing the input scaling matrix to provide more control authority is simpler than adjusting the weights, but removes some of the physical meaning in the weight selection.

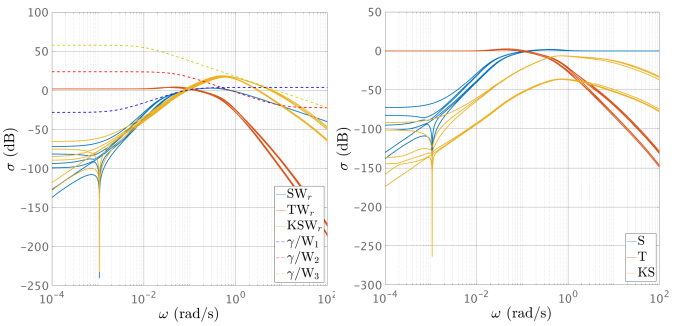

(a) (b)

Fig. 7. Scaled plant: SW_r, TW_r, and KSW_r at the plant output and their respective weights for $W_r \neq 1$. $\gamma = 0.77$ is achieved and the controller order is 42. (a) Scaled plant. (b) Unscaled plant.

IV. μ-Analysis

Necessary and sufficient conditions for the robust stability (RS) can be obtained using the SSVs or μ. The parameters which can bring uncertainties in the dynamics are the chaser mass, m_c, the inertias, I_c and I_t, the chaser fuel sloshing damping coefficient and natural frequency, c_s and f_s, and time delays. With a dry mass of 10 and 2 kg of fuel, the chaser total mass will vary throughout the mission between 10 and 12 kg

$$m_c = 11 \text{ kg } \pm 10\%. \tag{19}$$

The target mass uncertainty will not be considered as it does not carry any propellant, and can thus be precisely measured. CubeSats inertia tensors are usually not measured, rather estimated using available 3-D modeling software with an accuracy of ∼10%. Note that for the μ-analysis, the inertia tensors are assumed diagonal. This assumption is made to avoid repeated real parameters in Δ, which simplifies μ computation. As described in Section II-C, the damping coefficient and natural frequency of the fuel slosh are difficult parameters to estimate. For the model considered, as explained in [4], the following uncertainties will be assumed:

$$c_s = 0.33 \text{ s}^{-1} \pm 48\% \tag{20}$$

$$f_s = 0.025 \text{ Hz} \pm 40\%. \tag{21}$$

In Section III, the actuators' uncertainties were modeled by a diagonal matrix with the top-right term representing the forces'

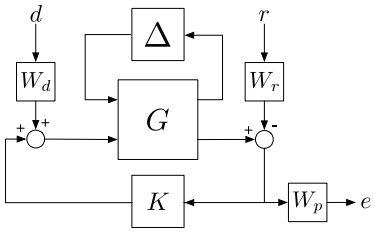

Fig. 8. Plant description used for the μ-analysis.

TABLE II
RELATIVE SENSITIVITY OF THE CONTROLLERS TO THE UNCERTAINTIES, IN% OF THE RP MARGIN

Δ	I_c	I_t	m_c	c_s	f_s	δ_τ	k_f	k_t	k_c
$\mathcal{H}_\infty$	2	2	26	49	4	37	36	14	21
μ-synthesis	3	1	20	72	12	67	31	11	17

effects on the torques. Here, it can be similarly modeled as

$$K_d = \begin{bmatrix} k_t & 0 & 0 & 0 & k_c & k_c \\ 0 & k_t & 0 & k_c & 0 & k_c \\ 0 & 0 & k_t & k_c & k_c & 0 \\ 0 & 0 & 0 & k_f & 0 & 0 \\ 0 & 0 & 0 & 0 & k_f & 0 \\ 0 & 0 & 0 & 0 & 0 & k_f \end{bmatrix} \tag{22}$$

with $k_f = k_t = 1 \pm 10\%$ and $k_c = 0 \pm 5\%$. K_d is a multiplicative gain at the plant input. Finally, a time delay is added at the plant input, lumping the multiple sources of delay present in the control loop into one single linear fractional transformation (LFT). The time delay transfer function is represented by a first-order Pad approximant. The control loop will be sampled at 1 Hz; the delay uncertainty δ_τ is estimated to be

$$\delta_\tau = 0.5 \text{ s } \pm 100\%. \tag{23}$$

Considering these uncertainties, the Δ-structure contains 53 real elements.

A. Robust Stability and Robust Performance

The μ-analysis diagram is shown in Fig. 8. As for the $\mathcal{H}_\infty$ synthesis, W_d is a diagonal matrix in which elements are all equal to 10^{-3}. This corresponds to the amount of orbital perturbations acting on the spacecraft (such as differential drag and gravity gradient) and not to the actuators errors, as these are already accounted for in the upper LFT. A performance weight W_p will be used to assess the sensitivity function behavior and has the same form as in (15). For W_p, the values for M_p and ω_p satisfying the requirement exactly are selected: $M_p = 2.5$, $\omega_p = 0.04$ rad/s, and $A_p = 0.05$ (see Section III-A). To compute the bounds of μ, a linear matrix inequality solver is used.

The value of μ for the RS and robust performance (RP) is shown in Fig. 9. The controller remains stable for 191% of the modeled uncertainties, and the closed-loop gain remains below one for 127%. For the RS, the steep drop at $\omega \approx 0.19$ rad/s is consistent with the controller crossover frequency. The

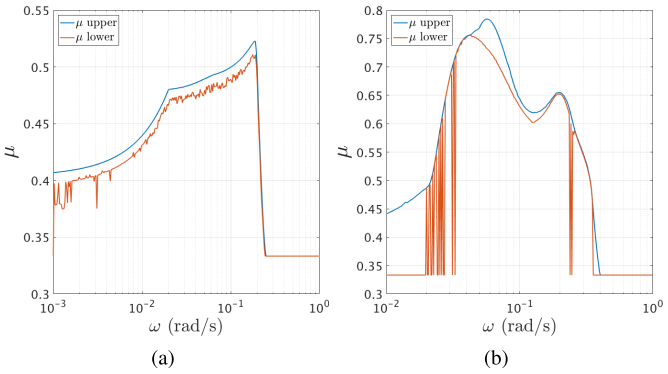

Fig. 9. (a) RS and (b) RP for the $\mathcal{H}_\infty$ controller.

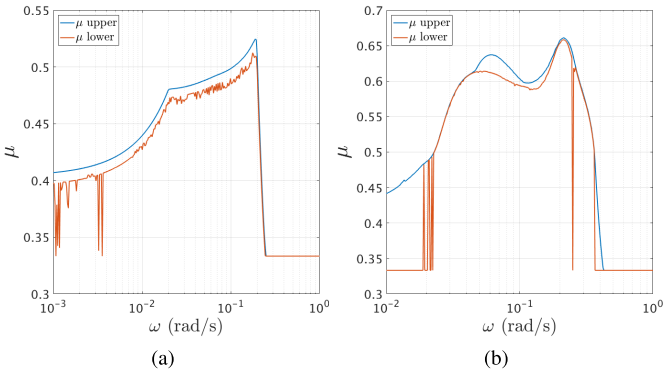

Fig. 10. (a) RS and (b) RP for the μ-synthesis controller.

RS is most sensitive to c_s at 99% and f_s at 63%. The RP sensitivity is summarized in Table II. The closed loop is barely sensitive to inertia uncertainties, which justifies the diagonal inertia assumption.

V. μ-SYNTHESIS

The μ-analysis performed in Section IV shows that the plant is most sensitive to the sloshing and actuators' uncertainties (22). Furthermore, as the sloshing model used in this brief is scaled at a CubeSat level but not tailored for it, increasing the robustness to these parameters is relevant. The Δ-structure for this case has dimension 28, with three occurrences for c_s, 16 for f_s, three for k_f, three for k_t, and three for k_t. It means that $\Delta \in \mathbb{R}$, and for real Δ-structure with repetitions, μ-synthesis is very unlikely to converge. The uncertain dynamic was thus approximated by a purely complex disturbance

$$G = G_{\text{nom}}(1 + W_\mu \Delta), \quad \Delta \in \mathbb{C}. \tag{24}$$

W_μ is computed using the MATLAB *ucover* command and is of order 5. Using the same scaling and weights as in the $\mathcal{H}_\infty$, a controller can be synthesized. The $D-K$ solver was initialized using the $\mathcal{H}_\infty$ controller previously obtained. It took nine iterations to reach a minimum, with $\gamma = 0.77$. The resulting controller order is 98 and its margins are at the input GM $= [-5.7, 8.36]$ dB, PM $= \pm 36°$, and $\omega_c = 0.21$ rad/s, and at the output GM $= [-12.8, 13.5]$ dB, PM $= \pm 46.4°$, and $\omega_c = 0.14$ rad/s. The RS and RP are using

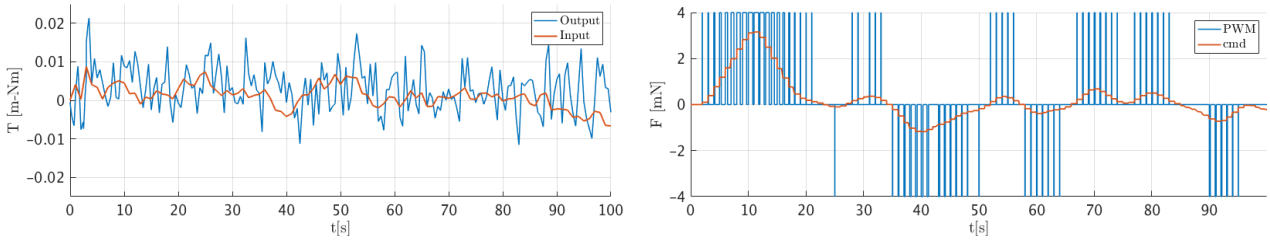

(a) (b)

Fig. 11. Torque and force commands and corresponding actuators' outputs. (a) Reaction wheels. (b) Propulsion.

the same weights and uncertainties than that described in Section IV. The μ values are shown in Fig. 10. This controller remains stable for 191% of the modeled uncertainties, and the closed-loop gain remains below one for 151%, which is indeed more than the $\mathcal{H}_\infty$. The sensitivity of the controller is provided in Table II.

VI. Nonlinear Simulation

The $\mathcal{H}_\infty$ controller order is 42, and the μ-synthesis is 98. Some of the controllers' poles have large negative real parts and can thus be removed, looking at the Hankel singular values. Using the MATLAB *balred* command, which is a balanced residualization preserving the dc gain, the $\mathcal{H}_\infty$ could be reduced to an order 30, and 43 for the μ-synthesis. For each controller, the closed-loop bandwidth is $\gtrsim$ 0.2 rad/s. To ensure a sampling frequency larger than ten times the bandwidth, the guidance, navigation, and control (GNC) is sampled at 1 Hz. The controllers are discretized using a bilinear transformation, which preserves the $\mathcal{H}_\infty$ norm [18].

Note that if the controllers' order would be an issue for implementation, another approach, called Structured-$\mathcal{H}_\infty$, which is the subject of a consequent amount of research, could also be used [19]–[21]. It benefits from the $\mathcal{H}_\infty$ framework, while at the same time, using low-order classical controllers with fixed structures.

The simulator used to assess the performances of the controllers was created in Simulink. It includes representative environmental, sensor, and actuator models, such as differential drag, gravity gradient, reaction wheels, propulsion, and star trackers. The propulsion is operated in PWM. The thrust time is computed as $T_{\text{ON}} = (u/u_{\max})T_{\text{PWM}}$ with $u_{\max}$ the maximum available control input and T_{PWM} the modulation period. The reaction wheels and propulsion outputs are provided in Fig. 11. Note that it has been proven that PWM adds time lead in the loop and thus does not degrade the robustness [22]. The target attitude pointing capability is shown in Fig. 12. The P2P VBN used for the docking and its capabilities are described in [15]. It provides a six-DoF solution and takes into account the coupling between rotations and translations.

For the ports' configuration described in Section II-D, the initial conditions for the chaser in $\mathcal{F}_\mathcal{O}$ are $\boldsymbol{s}_o^{ct} = [-5.2\ 0\ 0]^{\text{T}}$ m and $\boldsymbol{v}_o^{ct} = \boldsymbol{0}$, and $\mathcal{F}_{b_c}$ is aligned with $\mathcal{F}_\mathcal{O}$. For each Monte Carlo simulation, the uncertain parameters which have been described in Section IV are randomly generated.

At docking, the driving requirement is the lateral accuracy which shall be better than 5 mm (3σ). The number of Monte

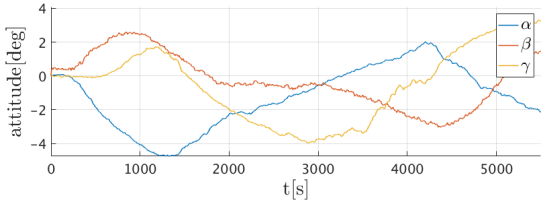

Fig. 12. Target attitude pointing accuracy.

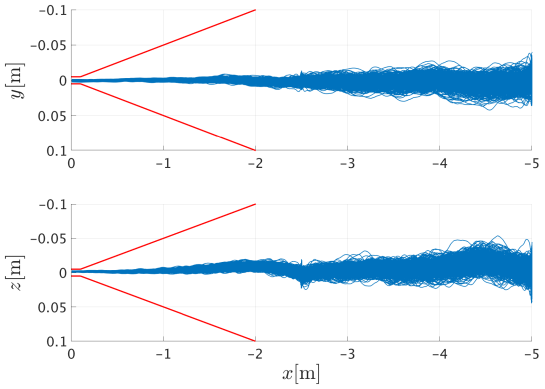

Fig. 13. $\mathcal{H}_\infty$: 600 Monte Carlo run. The red lines are the 5% of the range (3σ) requirement and the docking accuracy.

Carlo run was set to 600. This amount of simulation gives a 0.3-mm confidence interval on the 3σ requirement, with 95% confidence. Fig. 13 shows the $\mathcal{H}_\infty$ controller performances in the target docking frame $\mathcal{F}_{d_t}$. Note that at 2.5-m range along x, the chaser holds its position for 10 min before final docking. The translations are initiated by the guidance function which provides the acceleration profile as a feedforward directed to the propulsion system. To prevent saturation, the acceleration phases require only 2 mN of thrust (over 4 mN available). Recall that the approach speed is 1 cm/s.

All the simulated approaches for both controllers stay within the boundaries (depicted by the red lines in the figures). Fig. 14 shows the lateral accuracy at docking as well as the yaw and pitch angles. The red circles represent the 3σ requirements. All the simulations led to successful dockings with a 95% confidence. It can be seen that the μ-synthesis is slightly more accurate than the $\mathcal{H}_\infty$ due to its higher bandwidth. A systematic bias can be observed due to the relative dynamics. If required, this bias can be reduced by decreasing the value of A_1 in (15).

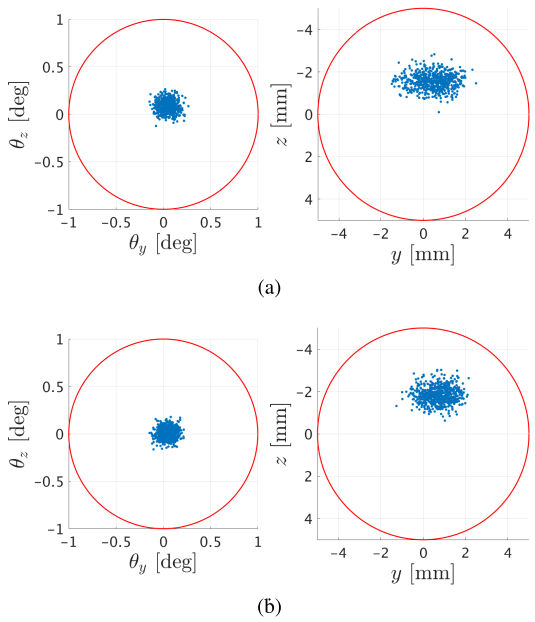

Fig. 14. Accuracy at docking for 600 Monte Carlo runs. The red circles are the 3σ requirements. (a) $\mathcal{H}_\infty$. (b) μ-synthesis.

VII. Conclusion

This brief aimed at assessing the feasibility of nanosatellites RVD, which was yet never achieved. Besides control accuracy which should be ten times better for CubeSats than for large satellites, the lower performances of the sensors and actuators make the task difficult. Two different controllers could be synthesized: $\mathcal{H}_\infty$ and μ-synthesis. Both controllers were shown, RS and RP, using μ-analysis, and as expected, the μ-synthesis exhibits higher robustness margins than the $\mathcal{H}_\infty$. Using nonlinear simulations, 600 Monte Carlo runs were performed, showing that both controllers satisfy the 5-mm (3σ) docking requirements with margins. Compared with other schemes, robust controllers provide a well-established framework to handle all the uncertainties, giving confidence in the results. Furthermore, having the μ-analysis closed-loop sensitivity at an early stage of a CubeSat mission design allows identifying critical elements to achieve a consistent systems' design. The proposed controllers together with the VBN are robust to wide range of uncertainties, and providing that the bounds on these uncertainties were indeed adequately identified, RVD between two CubeSats is feasible today.

References

[1] D. Pinard, S. Reynaud, P. Delpy, and S. E. Strandmoe, "Accurate and autonomous navigation for the ATV," *Aerosp. Sci. Technol.*, vol. 11, no. 6, pp. 490–498, Sep. 2007. [Online]. Available: http://www.sciencedirect.com/science/article/pii/S1270963807000624

[2] C. S. Pirat, P.-A. Mäusli, R. Walker, F. Ankersen, and V. Gass, "Guidance, navigation and control for autonomous cooperative docking of CubeSats," in *Proc. Small Satell. Syst. Services 4S Symp.*, Sorrento, Italy, May 2018, pp. 1–15. [Online]. Available: https://infoscience.epfl.ch/record/255877

[3] V. P. Legostayev and I. P. Shmyglevskiy, "Control of space vehicles rendezous at the stage of docking," *Automatica*, vol. 7, no. 1, pp. 15–24, Jan. 1971. [Online]. Available: http://www.sciencedirect.com/science/article/pii/0005109871900756

[4] F. Ankersen, "Guidance, navigation, control and relative dynamics for spacecraft proximity maneuvers," Ph.D. dissertation, Dept. Electron. Syst., Aalborg Univ., Aalborg, Denmark, 2011.

[5] E. J. Mora, J. B. Serrano, and F. Ankersen, "Mimo control for 6dof relative motion," in *Proc. Spacecraft Guid., Navigat. Control Syst., 3rd ESA Int. Conf.*, vol. 381, 1997, p. 219.

[6] C. Andrade *et al.*, "Robust control applied towards rendezvous and docking," in *Proc. Eur. Control Conf. (ECC)*, Aug. 2009, pp. 1854–1859.

[7] D.-R. Lee and H. Pernicka, "Integrated system for autonomous proximity operations and docking," *Int. J. Aeronautical Space Sci.*, vol. 12, no. 1, pp. 43–56, Mar. 2011. [Online]. Available: http://koreascience.or.kr/journal/view.jsp?kj=HGJHC0&py=2011&vnc=v12n1&% sp=43

[8] H. Park, S. Di Cairano, and I. Kolmanovsky, "Model predictive control of spacecraft docking with a non-rotating platform," *IFAC Proc. Volumes*, vol. 44, no. 1, pp. 8485–8490, 2011. [Online]. Available: http://www.sciencedirect.com/science/article/pii/S1474667016449736

[9] Q. Li, J. Yuan, B. Zhang, and C. Gao, "Model predictive control for autonomous rendezvous and docking with a tumbling target," *Aerosp. Sci. Technol.*, vol. 69, pp. 700–711, Oct. 2017. [Online]. Available: http://www.sciencedirect.com/science/article/pii/S1270963817301293

[10] M. G. Safonov, R. Y. Chiang, and H. Flashner, "H (infinity) robust control synthesis for a large space structure," *J. Guid., Control, Dyn*, vol. 14, no. 3, pp. 513–520, 1991, doi: 10.2514/3.20670.

[11] C. Charbonnel, "H∞ controller design and μ-analysis: Powerful tools for flexible satellite attitude control," in *Proc. AIAA Guid., Navigat., Control Conf.*, Toronto, Canada, 2010, doi: 10.2514/6.2010-7907.

[12] P. Simplício, S. Bennani, A. Marcos, C. Roux, and X. Lefort, "Structured singular-value analysis of the Vega launcher in atmospheric flight," *J. Guid., Control, Dyn.*, vol. 39, no. 6, pp. 1342–1355, Mar. 2016, doi: 10.2514/1.G000335.

[13] O. Montenbruck and E. Gill, *Satellite Orbits* (Models, Methods and Applications). Berlin, Germany: Springer-Verlag, 2000. [Online]. Available: https://www.springer.com/gb/book/9783540672807

[14] C. Pirat *et al.*, "Mission design and GNC for in-orbit demonstration of active debris removal technologies with CubeSats," *Acta Astronautica*, vol. 130, pp. 114–127, Jan./Feb. 2017. [Online]. Available: http://www.sciencedirect.com/science/article/pii/S0094576516301321

[15] C. Pirat, F. Ankersen, R. Walker, and V. Gass, "Vision based navigation for autonomous cooperative docking of CubeSats," *Acta Astronautica*, vol. 146, pp. 418–434, May 2018. [Online]. Available: http://linkinghub.elsevier.com/retrieve/pii/S0094576517309086

[16] S. Skogestad and I. Postlethwaite, *Multivariable Feedback Control: Analysis and Design*, 2nd ed. New York, NY, USA: Wiley, 2005. [Online]. Available: http://ieeexplore.ieee.org/iel5/37/4064830/04064853.pdf

[17] G. Balas, C. Richard, A. Packard, and S. Michael, "Robust control toolbox," MathWorks, Natick, MA, USA, Tech. Rep. R2017b, 2017.

[18] M. Green and D. J. N. Limebeer, *Linear Robust Control*. Upper Saddle River, NJ, USA: Prentice-Hall, 1995.

[19] R. S. da Silva de Aguiar, P. Apkarian, and D. Noll, "Structured robust control against mixed uncertainty," *IEEE Trans. Control Syst. Technol.*, vol. 26, no. 5, pp. 1771–1781, Sep. 2018.

[20] P. Apkarian and D. Noll, "Structured H-∞ control of infinite-dimensional systems," *Int. J. Robust Nonlinear Control*, vol. 28, no. 9, pp. 3212–3238, Jun. 2018, doi: 10.1002/rnc.4073.

[21] P. Gahinet and P. Apkarian, "Structured H-∞ synthesis in MATLAB," *IFAC Proc. Volumes*, vol. 44, no. 1, pp. 1435–1440, Jan. 2011. [Online]. Available: http://linkinghub.elsevier.com/retrieve/pii/S1474667016438115

[22] M. Ganet-Schoeller, J. Bourdon, and G. Gelly, *Non-Linear and Robust Stability Analysis for ATV Rendezvous Control*. Chicago, IL, USA: American Institute of Aeronautics and Astronautics, Aug. 2009, doi: 10.2514/6.2009-5951.